This is a repository copy of *Unified finite element methodology for gradient elasticity*.

Article:

Unified finite element methodology for gradient elasticity

Cristian Bagni[a,*], Harm Askes[a]

[a]*University of Sheffield, Department of Civil and Structural Engineering, Mappin Street, Sheffield S1 3JD, United Kingdom*

Abstract

In this paper a unified finite element methodology based on gradient-elasticity is proposed for both two- and three-dimensional problems, along with some considerations about the best integration rules to be used and a comprehensive convergence study. From the convergence study it has emerged that for both two and three-dimensional problems, the implemented elements show a convergence rate virtually equal to the corresponding theoretical values. Recommendations on optimal element size are also provided. Furthermore, the ability of the proposed methodology to remove singularities in statics has been demonstrated through a couple of examples, in both two and three dimensions.

Keywords: Finite element methodology; Gradient elasticity; Internal length scale; Fracture mechanics; Removal of singularity; 2D and 3D Finite elements

*Corresponding author. Tel.:+44(0)114 2227728; fax:+44(0)114 2227890

Email addresses: `c.bagni@sheffield.ac.uk` (Cristian Bagni), `h.askes@sheffield.ac.uk` (Harm Askes)

1. Introduction

Classical continuum theories are used to solve various fundamental engineering problems and applications. Even if these theories are capable of solving problems in which the scale of the unknowns is appreciable by the human eye, they have been used to characterise phenomena at a very small (atomistic) as well as extremely big (astronomic) scale. Furthermore, classical elasticity has also been recently applied to describe deformation problems at the micron and nano-scale.

Experimental observations have suggested that, at these two last scales of observation, classical continuum theories fail in the accurate description of deformation phenomena. In particular, classical theories produce singularities in the strain and stress fields, for example in correspondence of crack tips and dislocation lines. Furthermore, they are not able to capture size effects, even if the influence of size effects increases with the decrease of the component size.

The failure of classical continuum theories in the description of the above problems is linked to the absence of an internal length in the constitutive equations, representative of the underlying microstructure. To overcome the previously described deficiencies, it has been proposed to enrich the constitutive equations, through the introduction of high-order gradients of particular state variable (e.g. strains or stresses), accompanied by internal length parameters (see [1] for an overview).

The idea of using gradient elasticity to describe the mechanical behaviour of materials and structures dates back to the second half of the 19th century; however, the purpose of these theories has changed significantly over the

years (a comprehensive overview of the history of gradient elasticity can be found in [1]).

Despite its ability to overcome the deficiencies of classical elasticity in the solution of different problems, gradient elasticity has not found a significant diffusion in practical applications yet. One of the principal reasons is its non-trivial finite element implementation, mainly related to the continuity requirements imposed on the discretisation. In fact, while the standard equations of solid mechanics are usually second order partial differential equations (p.d.e.), the governing equations of gradient elasticity are typically fourth-order p.d.e.; this means that the discretisation of the gradient elasticity equations requires at least $\mathcal{C}^1$-continuous shape functions, instead of the usual $\mathcal{C}^0$-continuous shape functions, which cannot be straightforwardly defined and implemented in a finite element methodology.

There are two main approaches followed to implement gradient elasticity into a finite element methodology (for a more detailed overview see [1, 2]). The first one comprehends approaches that leave the continuum mechanics equations intact, by using Meshless methods [3–11], Penalty methods [12–14], Hermitian finite elements [15–18], next nearest neighbour interaction (instead of the simpler nearest neighbour interaction used in the standard finite element software) [19], etc. The second one includes approaches that transform the governing equations, in order to obtain less demanding continuity requirements; among these is the Ru-Aifantis theorem [20] which splits the original fourth-order p.d.e. in two uncoupled sets of second-order p.d.e.

In this paper, we build on the finite element technology developed by [2, 21] in that we use the aforementioned Ru-Aifantis theorem as a starting

point to develop a straightforward $\mathcal{C}^0$-continuous implementation. The work of these earlier papers is extended from 2D to 3D and higher-order elements, whilst also a comprehensive study of optimal numerical integration rules is provided and in-depth convergence studies have been carried out. Thus, recommendations on element types and sizes can now be made.

While in Section 2 the Ru-Aifants theory, implemented in the proposed methodology, is briefly reviewed, in Section 3 an effective $\mathcal{C}^0$ finite element implementation of this theory is described. Section 4 provides details about the best integration rules to use for each of the different implemented finite elements, whilst in Section 5 the convergence behaviours of the different implemented elements are compared and analysed for problems without singularities and in Section 6 the same has been done for a problem characterised by the presence of a singularity. Recommendations on optimal element size are also provided. In Section 7 original results, obtained by applying the proposed methodology to two different problems, are presented in order to demonstrate the ability of the methodology to remove singularities from the stress field for both two- and three-dimensional problems.

2. Ru-Aifantis theory of gradient elasticity

At the beginning of the 1990s, Aifantis and coworkers proposed to enrich the constitutive relations of classical elasticity by means of the Laplacian of the strain as [20, 22, 23]

$$\sigma_{ij} = C_{ijkl}(\varepsilon_{kl} - \ell^2 \varepsilon_{kl,mm}) \tag{1}$$

where σ_{ij} and ε_{kl} are, respectively, the stress and strain tensor, C_{ijkl} is the constitutive tensor and ℓ is a length scale parameter. The related equilibrium

4

equations are

$$C_{ijkl}(u_{k,jl} - \ell^2 u_{k,jlmm}) + b_i = 0 \tag{2}$$

where u_k is the displacement field and b_i are the body forces.

In a later work [20], Ru and Aifantis proposed an *operator split*, which allows the solution of the fourth-order equilibrium Eq. (2) as a decoupled sequence of two sets of second-order p.d.e., that is

$$C_{ijkl}u^c_{k,jl} + b_i = 0 \tag{3}$$

followed by the following reaction-diffusion equation

$$u^g_k - \ell^2 u^g_{k,mm} = u^c_k \tag{4}$$

that represents the relation between the local displacements u^c_i, obtained by solving the equations of classical elasticity Eq. (3) (carrying for this reason the superscript c), and the non-local displacements u^g_i, affected by the gradient activity (superscript g), which are the same displacements appearing in Eq. (2).

Substituting Eq. (4) into Eq. (3), the original Eq. (2) are recovered and imposing suitable boundary conditions the solution of Eqs. (3) and (4) coincides with that of the original Eq. (2). Nevertheless, the most interesting aspect of Eqs. (3) and (4) is their uncoupled format, which significantly simplifies both the analytical and numerical solution of the system of equations.

The first Ru-Aifantis approach introduces the gradient-enrichment in terms of displacements, as given in Eq. (4), but through a simple differentiation it is also possible to express the gradient-enrichment in terms of strains [2, 24, 25], that is

$$\varepsilon^g_{kl} - \ell^2 \varepsilon^g_{kl,mm} = \varepsilon^c_{kl} = \frac{1}{2}(u^c_{k,l} + u^c_{l,k}) \tag{5}$$

5

or stresses as [2, 26]

$$\sigma_{ij}^g - \ell^2 \sigma_{ij,mm}^g = C_{ijkl} u_{k,l}^c \tag{6}$$

3. Finite element implementation

As briefly explained in Section 2 and in more details in [1], the Ru-Aifantis theorem consists in solving two uncoupled sets of second-order p.d.e. instead of the original fourth-order p.d.e., which significantly simplifies the solution of the problem. From now on matrix-vector notation is adopted, instead of the index notation used in Section 2.

The first step of the Ru-Aifantis theory consists in determining the local displacements $\mathbf{u}^c$ by solving the second-order p.d.e. of classical elasticity:

$$\mathbf{L}^T \mathbf{C} \mathbf{L} \mathbf{u}^c + \mathbf{b} = 0 \tag{7}$$

where $\mathbf{b}$ are the body forces, $\mathbf{C}$ is the constitutive matrix, while the derivative operator $\mathbf{L}$ is defined as

$$\mathbf{L} = \begin{bmatrix} \frac{\partial}{\partial x} & 0 & 0 & \frac{\partial}{\partial y} & \frac{\partial}{\partial z} & 0 \\ 0 & \frac{\partial}{\partial y} & 0 & \frac{\partial}{\partial x} & 0 & \frac{\partial}{\partial z} \\ 0 & 0 & \frac{\partial}{\partial z} & 0 & \frac{\partial}{\partial x} & \frac{\partial}{\partial y} \end{bmatrix}^T \tag{8}$$

The continuum local displacements $\mathbf{u}^c = \begin{bmatrix} u_x^c, u_y^c, u_z^c \end{bmatrix}^T$ are expressed in terms of the nodal local displacements $\mathbf{d}^c = \begin{bmatrix} d_{1x}^c, d_{1y}^c, d_{1z}^c, d_{2x}^c, d_{2y}^c, d_{2z}^c, \dots \end{bmatrix}^T$ through the relation $\mathbf{u}^c = \mathbf{N_u} \mathbf{d}^c$, where $\mathbf{N_u}$ is the matrix which collects the

6

traditional shape functions N_i and can be written as:

$$\mathbf{N}_u = \begin{bmatrix} N_1 & 0 & 0 & N_2 & 0 & 0 & \dots \\ 0 & N_1 & 0 & 0 & N_2 & 0 & \dots \\ 0 & 0 & N_1 & 0 & 0 & N_2 & \dots \end{bmatrix} \tag{9}$$

Considering the finite element discretisation just described and integrating by parts, the weak form of Eq. (7) reads

$$\int_\Omega \mathbf{B}_u^T \mathbf{C} \mathbf{B}_u d\Omega \; \mathbf{d}^c \equiv \mathbf{K} \mathbf{d}^c = \mathbf{f} \tag{10}$$

where $\mathbf{K}$ is the stiffness matrix, $\mathbf{B}_u = \mathbf{L} \mathbf{N}_u$ is the strain-displacement matrix and $\mathbf{f}$ is the force vector, where the contributions of both the body forces and the external tractions are included.

At this point, knowing the local displacements $\mathbf{u}^c$ from the previous step, it is possible to evaluate the stress field by solving the second set of equations (second step):

$$(\boldsymbol{\sigma}^g - \ell^2 \nabla^2 \boldsymbol{\sigma}^g) = \mathbf{C} \mathbf{L} \mathbf{u}^c \tag{11}$$

where $\boldsymbol{\sigma}^g$ is the non-local stress tensor and the derivative operator ∇ is defined as

$$\nabla = \begin{bmatrix} \frac{\partial}{\partial x} \\ \frac{\partial}{\partial y} \\ \frac{\partial}{\partial z} \end{bmatrix} \quad \text{with} \quad \nabla^2 \equiv \nabla^T \nabla \tag{12}$$

Considering the weak form of Eq. (11) and integrating by parts, we obtain

$$\int_\Omega \left[\mathbf{w}^T \boldsymbol{\sigma}^g + \ell^2 \left(\frac{\partial \mathbf{w}^T}{\partial x} \frac{\partial \boldsymbol{\sigma}^g}{\partial x} + \frac{\partial \mathbf{w}^T}{\partial y} \frac{\partial \boldsymbol{\sigma}^g}{\partial y} + \frac{\partial \mathbf{w}^T}{\partial z} \frac{\partial \boldsymbol{\sigma}^g}{\partial z} \right) \right] d\Omega -$$
$$- \oint_\Gamma \mathbf{w}^T \ell^2 \left(\mathbf{n} \cdot \nabla \boldsymbol{\sigma}^g \right) d\Gamma = \int_\Omega \mathbf{w}^T \mathbf{C} \mathbf{L} \mathbf{u}^c d\Omega \tag{13}$$

7

where $\mathbf{n} = [n_x \ n_y \ n_z]^T$ contains the components of the normal vector to the boundary Γ and $\mathbf{w}$ is the test function vector.

Since the same finite element mesh can be used for both the first step, described above, and this second step, the same shape functions, previously used to discretise the displacements, can be used also for the discretisation of the stresses, making the solution of the problem much easier. Hence, the vector of the continuum non-local stresses $\boldsymbol{\sigma}^g$ is related to the vector of the nodal non-local stresses $\mathbf{s}^g$ through the relation $\boldsymbol{\sigma}^g = \mathbf{N}_\sigma \mathbf{s}^g$, where $\mathbf{N}_\sigma$ is an expanded form of the shape function matrix $\mathbf{N}_u$ given in Eq. (9), in order to accommodate all the non-local stress components.

Finally, using the same shape functions $\mathbf{N}_\sigma$ to discretise the test function vector $\mathbf{w}$ and recalling that $\mathbf{u}^c = \mathbf{N}_u \mathbf{d}^c$, the resulting system of equations reads

$$
\int_\Omega \left[\mathbf{N}_\sigma^T \mathbf{N}_\sigma + \ell^2 \left(\frac{\partial \mathbf{N}_\sigma^T}{\partial x} \frac{\partial \mathbf{N}_\sigma}{\partial x} + \frac{\partial \mathbf{N}_\sigma^T}{\partial y} \frac{\partial \mathbf{N}_\sigma}{\partial y} + \frac{\partial \mathbf{N}_\sigma^T}{\partial z} \frac{\partial \mathbf{N}_\sigma}{\partial z} \right) \right] d\Omega \ \mathbf{s}^g =
$$
$$
= \int_\Omega \mathbf{N}_\sigma^T \mathbf{C} \mathbf{B}_u d\Omega \ \mathbf{d}^c \tag{14}
$$

As can be noted, in passing from Eq. (13) to Eq. (14) the boundary integral $\oint_\Gamma \delta\boldsymbol{\sigma}^{gT} \ell^2 (\mathbf{n} \cdot \nabla \boldsymbol{\sigma}^g) \, d\Gamma$ has disappeared. This is due to the fact that

- if *essential* boundary conditions are used $\boldsymbol{\sigma}^g$ is known (usually the condition $\boldsymbol{\sigma}^g = \boldsymbol{\sigma}^c$ is chosen), therefore $\delta\boldsymbol{\sigma}^g = 0$;

- if *natural* boundary conditions are used the condition $\mathbf{n} \cdot \nabla\boldsymbol{\sigma}^g = 0$ is chosen.

Hence, either way the boundary integral cancels.

4. Numerical integration

To solve the first and second step of the Ru-Aifantis theory described above (i.e. Eqs. (10) and (14)) the Gauss quadrature rule has been adopted.

Since the first step of the Ru-Aifantis theory consists in the solution of the second-order p.d.e. of classical elasticity (10), for the numerical integration of the stiffness matrix $\mathbf{K}$, the usual number of integration points is used for each kind of implemented elements, as summarised in Table 1. It must be noted that for the bi-quadratic serendipity quadrilateral and the tri-quadratic serendipity brick elements, an under-integration is adopted.

Table 1. Number of Gauss points used in the first step of the Ru-Aifantis theory.

	Elements	Order	Gauss Points
2D Elements	Triangles	Linear	1
		Quadratic	3
	Quadrilaterals	Bi-linear	2×2
		Bi-quadratic	2×2
3D Elements	Tetrahedrons	Linear	1
		Quadratic	4
	Bricks	Tri-linear	$2 \times 2 \times 2$
		Tri-quadratic	$2 \times 2 \times 2$

At this point, the most interesting aspect to investigate is the integration rule to use in the second step of the Ru-Aifantis theory and, in particular, for the numerical solution of the integral in the left side of Eq. (14). The

most desirable solution would be, obviously, the possibility to use the same integration rule used in the first step of the Ru-Aifantis theory.

However, the applicability of such a solution is not obvious and would need to be demonstrated. In fact while for the first step of the Ru-Aifantis theory the order of the stiffness matrix (which has to be integrated) is two times the order of the derivative of the shape functions, in the second step the order of the integrand part (of the term in the left side of Eq. (14)) is two times the order of the shape functions themselves; this means that for exact integration, higher order integration rules are needed as listed in Table 2. Hence, in other terms, the problem is to prove if it is possible to under-integrate (i.e. use integration rules with a lower order than that necessary for the exact integration) the left part of Eq. (14) for both $\ell = 0$ and $\ell \neq 0$. Unfortunately, this is not always possible, as described afterwards.

The investigation has been carried out through a study of the eigenvalues of the matrix $\mathbf{M} + \ell^2 \mathbf{D}$ when $\ell \neq 0$ and, obviously, of matrix $\mathbf{M}$ on its own when $\ell = 0$, where $\mathbf{M} = \int_\Omega \mathbf{N}_\sigma^T \mathbf{N}_\sigma \, d\Omega$ is the first matrix term of the left integral in Eq. (14) similar to a mass matrix, while $\mathbf{D} = \int_\Omega \left(\frac{\partial \mathbf{N}_\sigma^T}{\partial x} \frac{\partial \mathbf{N}_\sigma}{\partial x} + \frac{\partial \mathbf{N}_\sigma^T}{\partial y} \frac{\partial \mathbf{N}_\sigma}{\partial y} + \frac{\partial \mathbf{N}_\sigma^T}{\partial z} \frac{\partial \mathbf{N}_\sigma}{\partial z} \right) d\Omega$ is the second matrix term similar to a diffusivity matrix. In particular, to avoid rank deficiencies all the eigenvalues must be non-zero, which means that zero energy modes are not admitted.

From the performed studies it turned out that, when $\ell = 0$, it is possible to use the same integration rule only for the linear quadrilateral, tetrahedron and brick elements, while for the other five types of elements higher order integration rules are needed (the minimum number of integration points is given in Tab. 2, for each kind of element). On the contrary, for $\ell \neq 0$, thanks

to the contribution of the matrix $\mathbf{D}$, it is possible to use the same integration rule, used in the first step, for every type of finite element.

Table 2. Number of Gauss points formally required in the second step of the Ru-Aifantis theory.

	Elements	Order	Gauss Points
2D Elements	Triangles	Linear	3
		Quadratic	6 (degree of precision 4)
	Quadrilaterals	Bi-linear	2×2
		Bi-quadratic	3×3
3D Elements	Tetrahedrons	Linear	1
		Quadratic	11
	Bricks	Tri-linear	$2 \times 2 \times 2$
		Tri-quadratic	$3 \times 3 \times 3$

4.1. Shear locking

As well known, in the case of bending-dominant problems, especially for fully integrated linear elements, the numerical solution of the problem can be affected by shear locking, leading to an unphysically stiffer behaviour of the analysed component. To check the occurrence of this phenomenon, the proposed methodology has been applied to model a classical bending problem. The results of the aforementioned analysis have shown that the numerical solution of the second step of the Ru-Aifantis theory (Eq. (14)) is not affected by locking effects, even in the case of fully integrated linear elements, while the usual selective integration rules may be applied for the first step (Eq. (10)).

5. Error estimation and convergence study

Now that the most suitable integration rules have been identified for each kind of finite element, the attention can be focused on the error estimation of the new methodology; in particular the convergence rate of the different finite elements has been studied for some simple problems.

To determine the convergence rate, the L2-norm error defined as

$$\|e\|_2 = \frac{\|\sigma_e - \sigma_c\|}{\|\sigma_e\|} \tag{15}$$

where σ_e and σ_c are, respectively, the exact and calculated values of the stresses, has been plotted against the number of degrees of freedom (nDoF).

From the theory [27] it is well known that the error on displacements is proportional to the nDoF as

$$e_u \simeq O(\text{nDoF})^{-\frac{n+1}{k}} = O(\text{nDoF})^{\text{p}} \tag{16}$$

For what concerns the stresses, in the proposed methodology they are calculated from Eq. (14) as primary variable, instead of secondary variable as it happens in standard finite element methodologies, based on classical elasticity. For this reason, the error on stresses is still proportional to the nDoF, but with a different rate respect to classical elasticity. In particular, for a Helmholtz equation like Eq. (14), the proportionality is given by [28]:

$$e_\sigma \simeq O(\text{nDoF})^{-\frac{n+1}{k}} = O(\text{nDoF})^{\overline{\text{p}}} \tag{17}$$

where n is the polynomial order and $k = 2, 3$ for 2D and 3D problems, respectively.

From Eqs. (16) and (17) , it is clear that the $\|e\|_2 - \text{nDoF}$ curve in a

bi-logarithmic system of axes is a straight line, whose slope represents the convergence rate p of the numerical solution to the exact solution. The theoretical convergence rates are summarised in Table 3.

Table 3. Theoretical convergence rates in the determination of the displacements (p) and stresses $(\bar{p})$.

	Order	p	$\bar{p}$
2D Problems	Linear	-1	-1
	Quadratic	-3/2	-3/2
3D Problems	Linear	-2/3	-2/3
	Quadratic	-1	-1

5.1. Internally pressurised hollow cylinder

To test the convergence rate of the bi-dimensional elements, the problem of a cylinder subjected to an internal pressure p_i shown in Fig. 1 has been analysed. The geometrical and material parameters of the problem are $b = 4$ m, $a = 1$ m, $E = 10^9$ N/m^2, $\nu = 0.25$ and $\ell = 0.1$ m. An internal pressure $p_i = 10^7$ N/m^2 is applied.
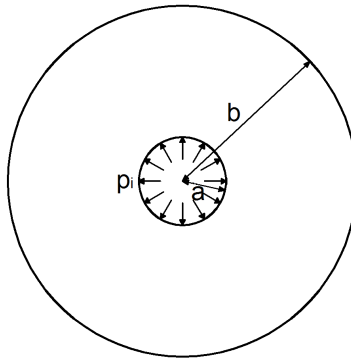

Fig. 1. Cylinder subject to an internal pressure: geometry and loading conditions.

Due to the symmetry of the problem only a quarter of the vessel has been modelled. The domain has been modelled with all four types of implemented 2D finite elements, starting from a coarse mesh of 8×8 elements and performing then a mesh refinement by doubling the number of elements along each side until a mesh of 256×256 elements is obtained. All the employed meshes are shown in Fig. 2.

The boundary conditions accompanying Eq. (10) are taken as *homogeneous essential* so that the circumferential displacements u_θ are null along the two axes of symmetry, while those associated to Eq. (14) are chosen as *homogeneous natural* throughout, that is $\mathbf{n} \cdot \nabla \boldsymbol{\sigma}^g = 0$.
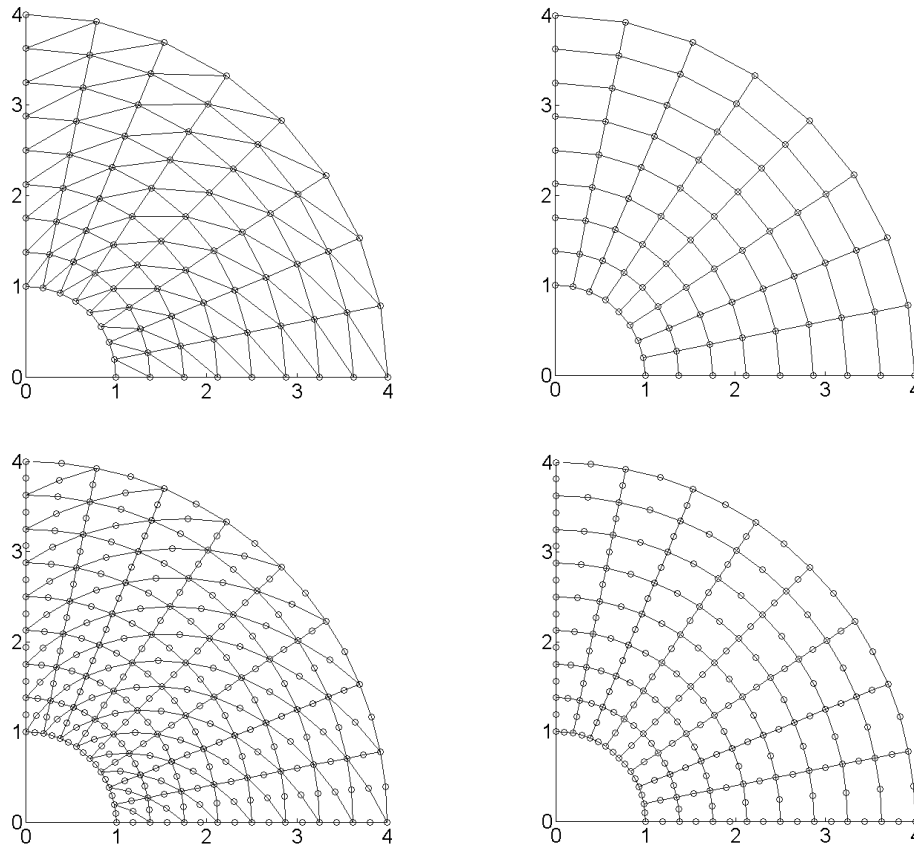
Fig. 2. Cylinder subject to an internal pressure: employed meshes for linear (top-left) and quadratic (bottom-left) triangular elements, bi-linear (top-right) and bi-quadratic (bottom-right) quadrilateral elements.

To define the error, the numerical solutions obtained using the new methodology have been compared with the exact solution approximated using Richardson extrapolation [29].
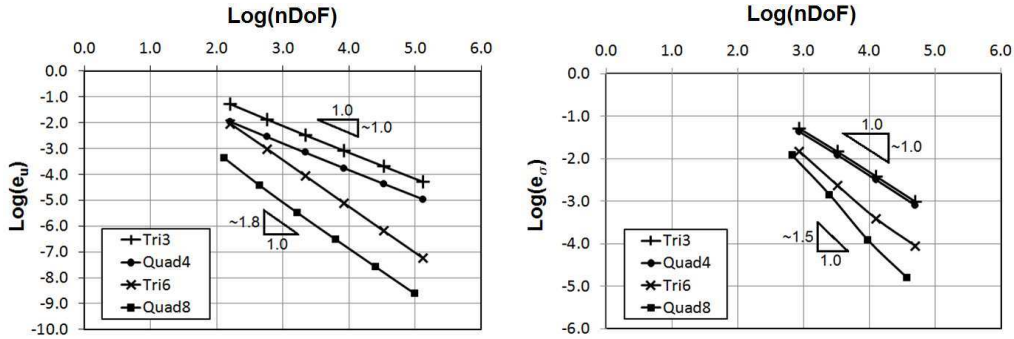
Fig. 3. Cylinder subject to an internal pressure: displacements error (left) and stresses error (right) versus number of Degrees of Freedom. The slope of the straight lines represents the convergence rate of the numerical solution to the exact solution.

In Fig. 3 the convergence behaviour of all the implemented bi-dimensional elements is shown, for both displacements and stresses. It can be seen that the numerically obtained convergence rates are in good agreement with the theoretical predictions given in Table 3.

5.2. Cross-shape specimen

The second problem is the case of a cross-shape specimen subjected to a uniform tensile state at the end of the arms as shown in Fig. 4. The geometrical and material parameters of the problem are R = 1 m, L = 2 m, E = 10^9 N/m^2, ν = 0.25 and ℓ = 0.1 m. Distributed loads q$_x$ = q$_y$ = 1000 N/m are applied at the end of the arms.
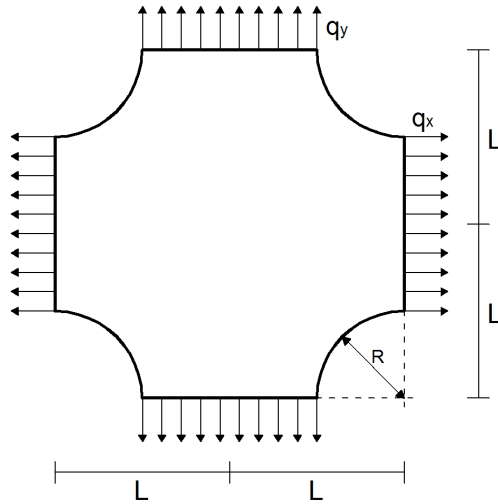
16

Fig. 4. Cross-shape specimen: geometry and loading conditions.

Also in this case, for symmetry reasons, only a quarter of the specimen has been modelled using all the different types of finite elements implemented, starting also in this case with a coarse mesh as shown in Fig. 5. Afterwords, a mesh refinement has been performed, running four other meshes obtained doubling the number of elements, in both radial and circumferential directions, of the previous one.

The boundary conditions accompanying Eq. (10) are taken as *homogeneous essential* so that the displacements in x-direction u_x and in y-direction u_y are null along the vertical and horizontal axes of symmetry, respectively. For what concerns Eq. (14), instead, the boundary conditions are chosen as *homogeneous natural* throughout, like in the previous example.
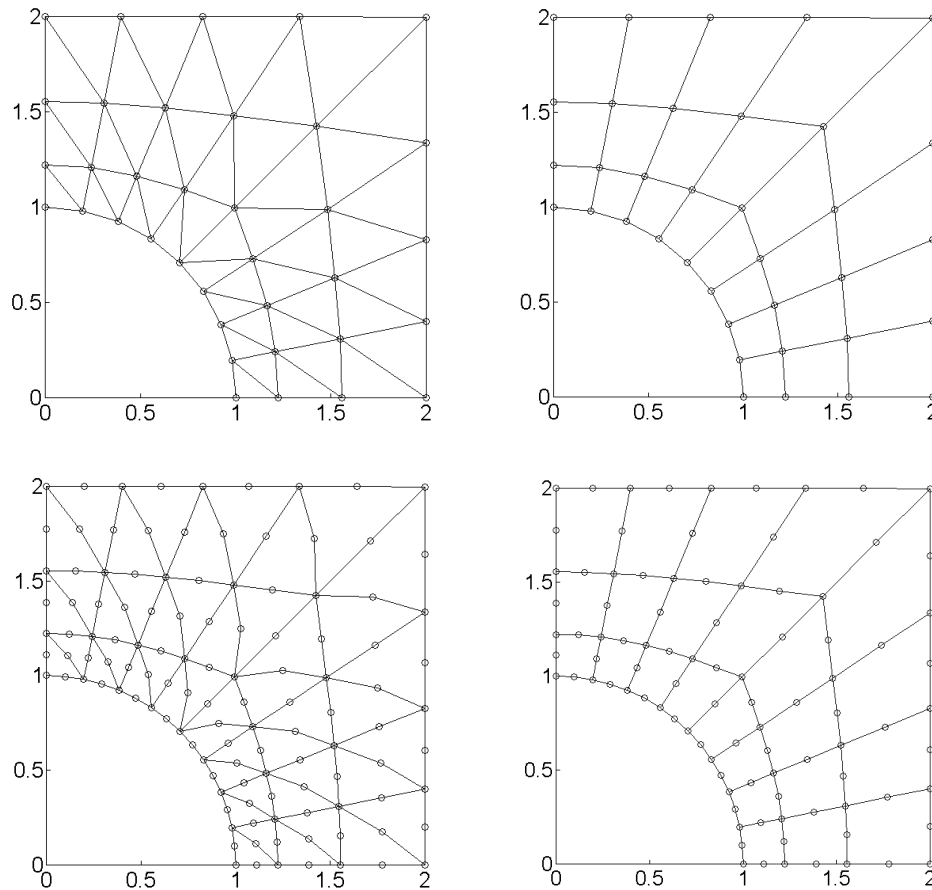
17

Fig. 5. Cross-shape specimen: employed meshes for linear (top-left) and quadratic (bottom-left) triangular elements, bi-linear (top-right) and bi-quadratic (bottom-right) quadrilateral elements.

To define the error, the numerical solutions obtained using the new methodology have been compared with the exact solution obtained applying the Richardson extrapolation.
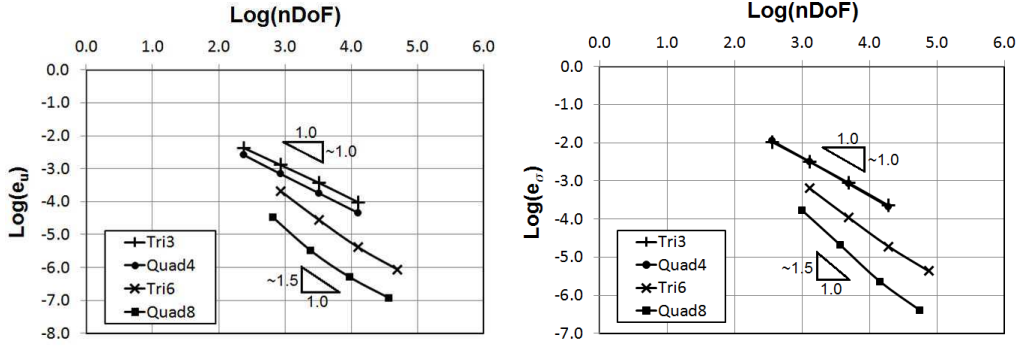
18

Fig. 6. Cross-shape specimen: displacements error (left) and stresses error (right) versus number of Degrees of Freedom. The slope of the straight lines represents the convergence rate of the numerical solution to the exact solution.

Fig. 6 shows the convergence behaviour of all the implemented bi-dimensional elements in the determination of both displacements and stresses; again, this is in line with the theoretical predictions.

5.3. Internally pressurised hollow sphere

For what concerns the convergence rate of the three-dimensional elements, the problem of a sphere subjected to an internal pressure p_i shown in Fig. 7 has been studied. The geometrical and material parameters of the problem are $b = 1$ m, $a = 0.5$ m, $E = 10^9$ N/m², $\nu = 0.25$ and $\ell = 0.1$ m. An internal pressure $p_i = 10^7$ N/m² is applied.

Due to the symmetry of the problem only an eighth of the sphere has been modelled. The domain has been modelled with all four types of implemented 3D finite elements, starting from a coarse mesh, as shown in Fig. 7 for the tri-linear brick elements, and performing then a uniform mesh refinement.

The boundary conditions related to Eq. (10) are taken as *homogeneous essential* so that the circumferential displacements are null on the three planes

19

of symmetry, while for what concerns Eq. (14) they are chosen as *homogeneous natural* throughout, like in the previous two examples.
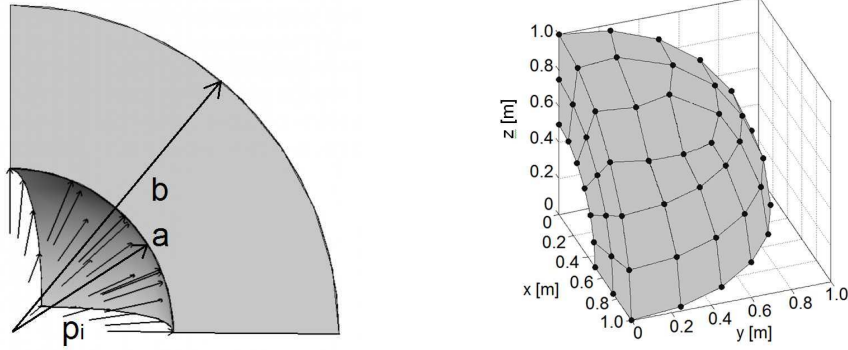

Fig. 7. Hollow sphere subject to an internal pressure: geometry and loading conditions (left), initial mesh (right).

To define the error, the numerical solutions obtained using the new methodology have again been compared with the exact solution obtained applying the Richardson extrapolation.
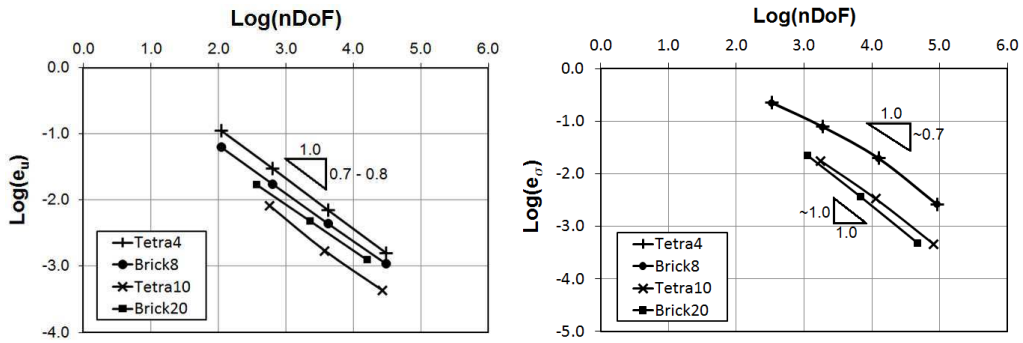

Fig. 8. Hollow sphere subject to an internal pressure: displacements error (left) and stresses error (right) versus number of Degrees of Freedom. The slope of the straight lines represents the convergence rate of the numerical solution to the exact solution.

Fig. 8 shows the convergence behaviour of all the implemented three-dimensional

elements in the determination of both displacements and stresses. It can be observed that, overall, the numerical solutions converge to the relative exact solutions as theoretically expected, except for the quadratic tetrahedrons and the tri-quadratic bricks, which appear to be slightly, but not much, slower than theoretically predicted, in the determination of the displacements.

6. Convergence in presence of singularities and recommendations on optimum element size

As mentioned in Section 1, one of the features of gradient elasticity is the ability to remove singularities from the stress and strain fields as those emerging in correspondence of crack tips. Problems characterised by the presence of cracks represent the most demanding case from the convergence point of view and, as a consequence of this, also in terms of element size in the vicinity of the crack tip. Hence, the study of the convergence behaviour of the implemented gradient-enriched finite elements in presence of cracks is of prime importance.

To fulfil this interest, the mode I fracture problem shown in Fig. 9 and presented in [1] has been analysed, using all the four implemented two-dimensional elements. The geometrical and material parameters of the problem are $L = 1$ mm, $E = 1000$ N/mm^2, $\nu = 0.25$ and $\ell = 0.1$ mm. Prescribed displacements $\overline{u} = 0.01$ mm are applied at the top and bottom edges. Due to the symmetry only the top-right quarter has been modelled, with 4×4, 8×8, 16×16, 32×32 and 64×64 bi-linear and bi-quadratic quadrilateral elements and with the double of linear and quadratic triangular elements (where the triangular mesh is obtained by subdividing each quadrilateral element into
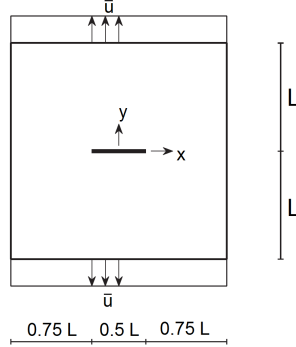
two triangles).

Fig. 9. Mode I fracture problem: geometry and boundary conditions. The crack is represented by the solid line.

Two different options are considered for the boundary conditions accompanying Eq. (13):

- **Option 1**: *essential*, that is the non-local stress components are prescribed so that $\boldsymbol{\sigma}^g = \boldsymbol{\sigma}^c$ on free boundaries. In the present example: $\sigma_{xx}^g = 0$ on the vertical edges, $\sigma_{yy}^g = 0$ on the face of the crack and $\sigma_{xy}^g = 0$ everywhere.

- **Option 2**: *homogeneous natural* throughout, that is $\mathbf{n} \cdot \nabla \boldsymbol{\sigma}^g = 0$.

To determine the convergence rate, the L2-norm error defined in Section 5 has been plotted against the nDoF, as shown in Fig. 10.

From the theory [27] it is well known that, in problems with singularities, the error on classical stresses is proportional to the nDoF as

$$e_\sigma \simeq O(\text{nDoF})^{-[\min(\lambda, n)]/2} = O(\text{nDoF})^{\tilde{p}} \tag{18}$$

where $\lambda = 0.5$ for a nearly closed crack.

From Eq. (18), it is clear that the $\|e\|_2 - \text{nDoF}$ curve in a bi-logarithmic

22

system of axes is still a straight line, whose slope represents the convergence rate $\tilde{p}$ of the numerical solution to the exact solution, which in this case is $\tilde{p} = 0.25$ for both linear and quadratic elements.

To define the error, the numerical solutions obtained using the new methodology have been compared with the exact solution approximated using Richardson extrapolation.

Fig. 10 shows that, in presence of singularities, both linear and quadratic elements are characterised by approximatively the same convergence rate (in accordance with Eq. (18)), but higher than the correspondent theoretical value defined in Eq. (18), for what concerns the determination of the stresses. This higher convergence rate is due to two main causes:

- removal of singularities from the numerical solution;

- gradient-enriched stresses calculated as primary variables, instead of secondary variables (as for classical stresses).

Furthermore, it can be observed that, while the application of the second option of the boundary conditions leads to a uniform convergence rate equal to about 0.8, adopting the first option all the elements are characterised by an initial convergence rate of about 0.3, reaching the same convergence rate obtained using the option 2 only for more refined meshes.
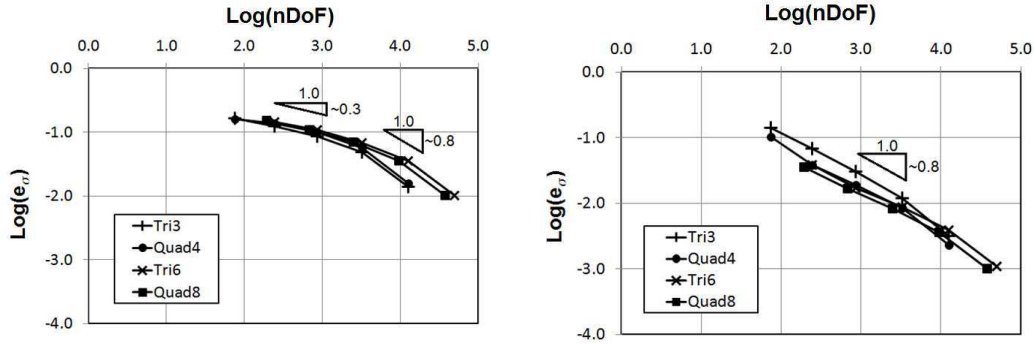
Fig. 10. Mode I fracture problem: stresses error versus number of Degrees of Freedom for the first (left) and the second (right) option of boundary conditions. The slope of the straight lines represents the convergence rate of the numerical solution to the exact solution.

Since, as mentioned before, the case of a sharp crack represents the most demanding problem in terms of convergence, it is now possible to provide recommendations on optimal element size. In particular, in Table 4 the ratio between the element size and the length scale ℓ, necessary to guarantee an error of about 5% or lower, is summarised for the different elements.

The recommendations provided in Table 4 have a very important meaning from the commercial point of view, because they show that, applying the proposed methodology, a relatively coarse mesh is enough to obtain a solution affected by an acceptable error, with evident benefits in terms of computational cost.

24

Table 4. Recommended optimal element size, to guarantee an error of 5% or lower.

Boundary Conditions	Elements	Order	Element size/ℓ
Option 1 (essential b.c.)	Triangles	Linear	1/3
		Quadratic	1/4
	Quadrilaterals	Bi-linear	1/3
		Bi-quadratic	1/3
Option 2 (natural b.c.)	Triangles	Linear	1
		Quadratic	5/2
	Quadrilaterals	Bi-linear	3/2
		Bi-quadratic	5/2

7. Applications

Once the new methodology was fully implemented, it has been applied to a two- and three-dimensional problem, in order to show the ability of the methodology in removing singularities.

7.1. Mode I fracture

The mode I fracture problem described in Section 6 has been analysed, using all the four implemented two-dimensional elements, in order to check the quality of the results.

In Fig. 11 σ_{xx} and σ_{yy} profiles along the x-axis, obtained applying both the options on the boundary conditions, are plotted and compared; it can be seen that the application of the different boundary conditions produces almost no variations for σ_{xx} and moderate but acceptable effects on σ_{yy}.
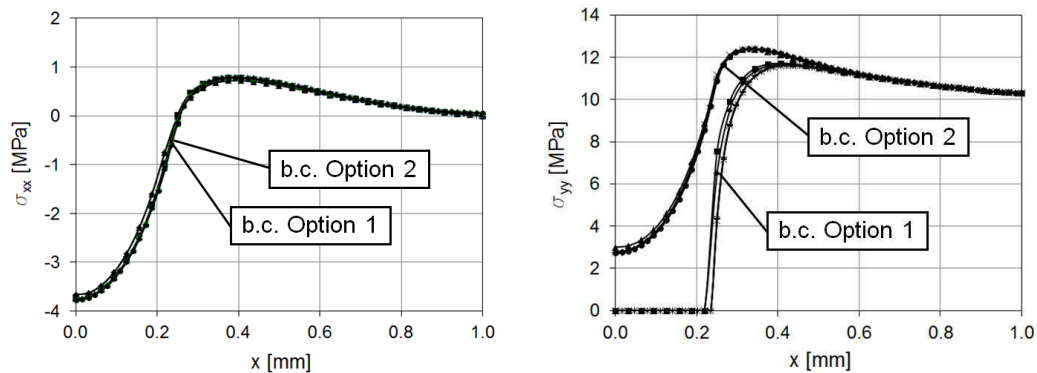
Fig. 11. Mode I fracture problem: comparison of the σ_{xx} (left) and σ_{yy} (right) values for $y = 0$, obtained employing the different kind of finite elements and both the options for the boundary conditions.
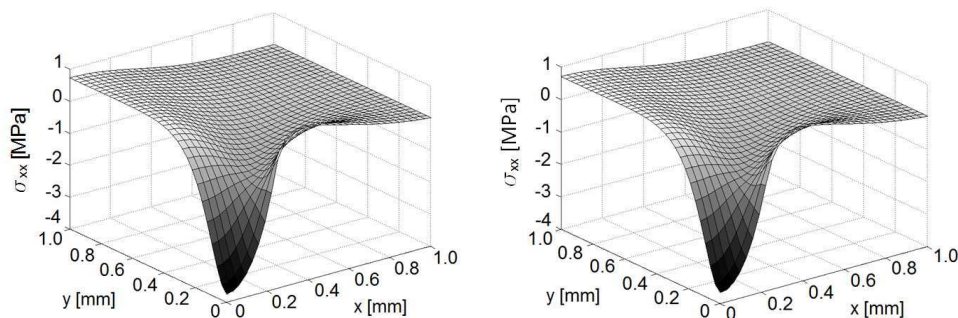

Fig. 12. Mode I fracture problem: surface plots of stress component σ_{xx} with *homogeneous essential* boundary conditions. Comparison between the results obtained in [1] using bi-linear quadrilateral elements (left) and those obtained employing the implemented linear triangular elements (right).

The stress fields obtained using the 32×32 mesh, with all the four types of elements, have been compared with the stress fields presented in [1] using 32×32 bi-linear quadrilateral elements and, as shown in Fig. 12, the employment of the different types of finite elements produces comparable results

(in Fig. 12 only the σ_{xx} field, obtained using the linear triangular elements and the second option for the boundary conditions, is compared with the corresponding one presented in [1]).

But the most significant aspect is that, introducing a gradient enrichment, the singularities in the stress field are removed; in fact, as shown in Fig. 13, applying classical elasticity the solution does not converge to a finite value upon mesh refinement and an unbounded peak is detected in correspondence of the crack tip, while introducing a gradient enrichment in the governing equations, refining the mesh the solution is not anymore singular and converges towards a unique finite value.
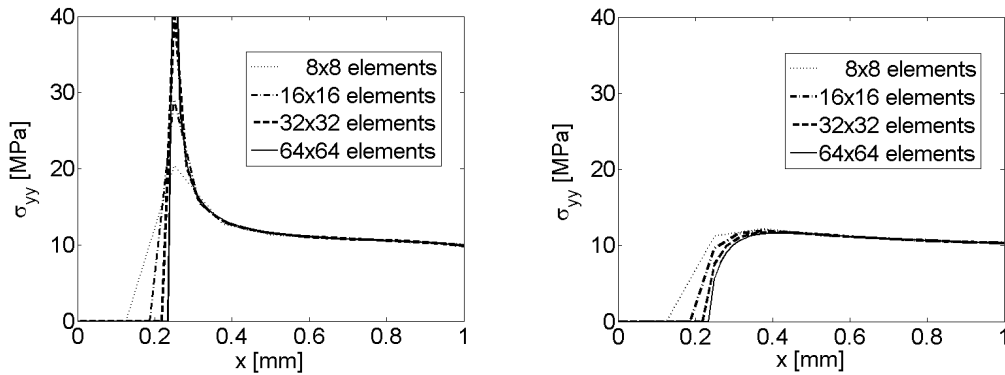

Fig. 13. Mode I fracture problem: σ_{yy} profiles along x-axis obtained by applying classical elasticity (left) and gradient elasticity (right) and the first option on the boundary conditions, upon mesh refinement.

7.2. Beams-column joint

In order to show the ability of the proposed methodology to remove the singularities also in three-dimensional problems, the problem shown in Fig. 14 has been studied. The geometrical and material properties of the problem

are $L = 2.4$ m, $a = 0.4$ m, $E = 1000$ N/mm², $\nu = 0.25$ and $\ell = 0.03$ m. Prescribed surface distributed loads $q = 10^5$ N/m² are applied at the free end of the two beams, while the column is fully restrained at its base. The boundary conditions associated to Eq. (14) are chosen as *homogeneous natural* throughout, that is $\mathbf{n} \cdot \nabla \boldsymbol{\sigma}^g = 0$. The domain has been modelled using 128 (Fig. 14), 1024, 8192 and 65536 linear brick elements.
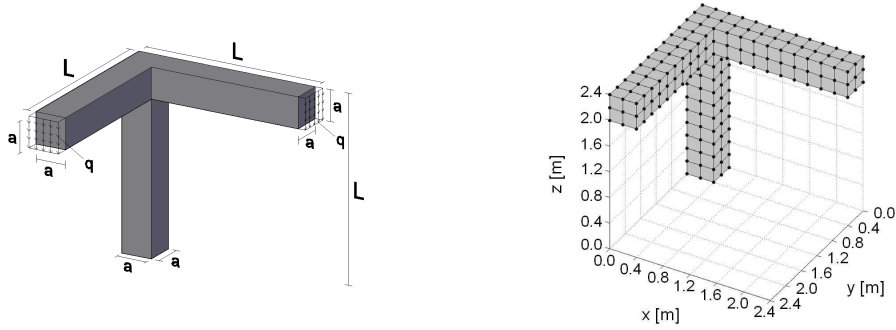

Fig. 14. Beams-column joint: geometry and loading conditions (left), starting mesh (right).

In Fig. 15 the normal stress σ_{xx} and the shear stress σ_{xy} obtained by applying both classical elasticity ($\ell = 0.00m$) and gradient elasticity ($\ell = 0.03m$) are plotted along a vertical edge of the column ($x = 0.4$, $y = 0.4$, $0.0 \leq z \leq 2.4$), while in Fig. 16 the normal stress σ_{xx} is plotted along the beam in y-direction ($x = 0.2$, $0.0 \leq y \leq 2.4$, $z = 2.0$).
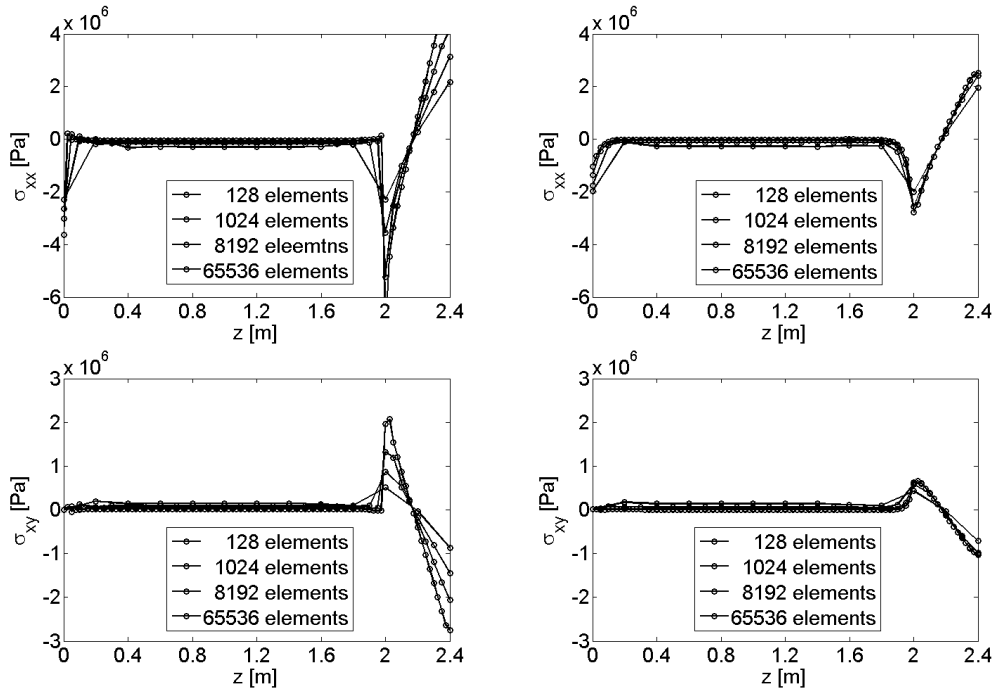
28

Fig. 15. Beams-column joint: profiles of σ_{xx} (top row) and σ_{xy} (bottom row), along a column vertical edge ($x = 0.4$, $y = 0.4$, $0.0 \leq z \leq 2.4$), for both classical (left column) and gradient (right column) elasticity, over mesh refinement.
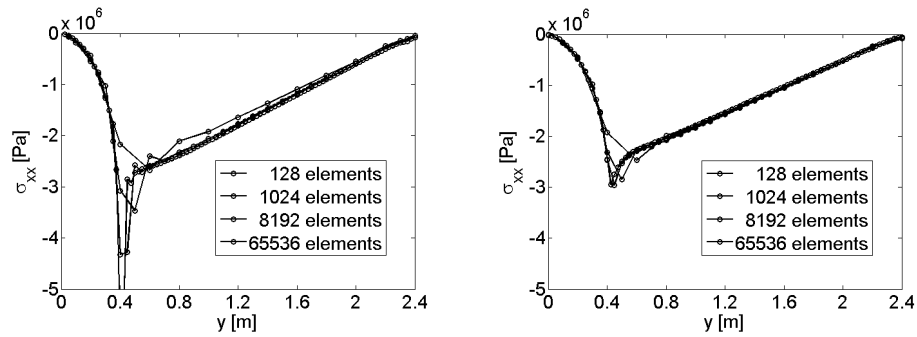

Fig. 16. Beams-column joint: profiles of σ_{xx}, along the beam in y-direction ($x = 0.2$, $0.0 \leq y \leq 2.4$, $z = 2.0$), for both classical (left column) and gradient (right column) elasticity, over mesh refinement.

29

Both figures clearly show the ability of the proposed methodology to remove singularities from the stress fields; in fact while the use of classical elasticity leads to singular solutions in correspondence of the stress concentrators, if a gradient enrichment is introduced in the governing equations of the problem, the solutions are not singular anymore, converging to a unique finite solution. Hence the ability of the proposed methodology to remove the singularities is confirmed also for three dimensional problems.

8. Conclusions

In this paper a unified FE methodology based on gradient-elasticity, for both two- and three-dimensional finite elements, has been presented, including Gauss integration rules and error estimation.

The proposed methodology has been applied to both two- and three-dimensional simple problems without singularities and it has been found that, overall, the numerically obtained convergence rates are well in line with theoretical predictions.

The convergence rate of the proposed methodology has been also analysed in presence of singularities, showing that both linear and quadratic elements are characterised by a convergence rate higher than the theoretical value typical of finite element methodologies based on classical elasticity. This is mainly due to the ability of gradient elasticity to remove singularities from the numerical solution and to the fact that, in the proposed methodology, the gradient-enriched stresses are determined as primary variables, instead of secondary variables as for classical elasticity-based finite element methodologies. Moreover, recommendations on optimal element size have

been provided, highlighting the ability of the proposed methodology to produce solutions affected by acceptable errors using relatively coarse meshes, with consequent advantages in terms of computational cost.

Furthermore, the proposed methodology has been applied to a couple of problems that classical elasticity fails to describe accurately, in particular to a two-dimensional mode I fracture problem, through which it has been shown that the different implemented finite elements produce comparable results (as expected) and that the application of different boundary conditions leads to limited and acceptable differences in the final solution; and to a three-dimensional problem characterised by stress concentrators. These two examples highlight the ability of the proposed methodology to remove the singularities from the stress fields, for both two- and three-dimensional problems.

Acknowledgements

References

[1] H. Askes and E. C. Aifantis. Gradient elasticity in statics and dynamics: An overview of formulations, length scale identification procedures, finite element implementations and new results. *International Journal of Solids and Structures*, 48(13):1962–1990, 2011. doi: 10.1016/j.ijsolstr.2011.03.006.

[2] H. Askes, I. Morata, and E. C. Aifantis. Finite element analysis with staggered gradient elasticity. *Computers & Structures*, 86:1266–1279, 2008. doi: 10.1016/j.compstruc.2007.11.002.

[3] H. Askes, J. Pamin, and R. de Borst. Dispersion analysis and element-free Galerkin solutions of second- and fourth-order gradient-enhanced damage models. *International Journal for Numerical Methods in Engineering*, 49:811–832, 2000.

[4] H. Askes and E. C. Aifantis. Numerical modelling of size effects with gradient elasticity - formulation, meshless discretization and examples. *International Journal of Fracture*, 117:347–358, 2002.

[5] H. Askes and L. J. Sluys. Explicit and implicit gradient series in damage mechanics. *European Journal of Mechanics - A/Solids*, 21:379–390, 2002.

[6] H. Askes, A.S.J. Suiker, and L. J. Sluys. A classification of higher-order strain-gradient models - linear analysis. *Archive of Applied Mechanics*, 72:171–188, 2002.

[7] H. Askes and L. J. Sluys. A classification of higher-order strain-gradient models in damage mechanics. *Archive of Applied Mechanics*, 73:448–465, 2003.

[8] J. Pamin, H. Askes, and R. de Borst. Two gradient plasticity theories discretized with the element-free Galerkin method. *Computer Methods in Applied Mechanics and Engineering*, 192:2377–2403, 2003. doi: 10.1016/S0045-7825(03)00263-9.

[9] Z. Tang, S. Shen, and S.N. Atluri. Analysis of materials with strain-gradient effects: a meshless local Petrov-Galerkin (MLPG) approach, with nodal displacements only. *Computer Modeling in Engineering & Sciences*, 4:177–196, 2003.

[10] I. Tsagrakis and E. C. Aifantis. Element-free Galerkin implementation of gradient plasticity. Part I: formulation and application to 1D strain localization. *Journal of the Mechanical Behavior of Materials*, 14:199–231, 2003.

[11] I. Tsagrakis and E. C. Aifantis. Element-free Galerkin implementation of gradient plasticity. Part II: applications to 2D strain localization and size effects. *Journal of the Mechanical Behavior of Materials*, 14:233–253, 2003.

[12] J. Pamin. *Gradient-dependent plasticity in numerical simulation of localization phenomena*. Dissertation, Delft University of Technology, 1994.

[13] A. Zervos. Finite elements for elasticity with microstructure and gradient elasticity. *International Journal for Numerical Methods in Engineering*, 73(4):564–595, 2008. doi: 10.1002/nme.2093.

[14] A. Zervos, S. Papanicolopulos, and I. Vardoulakis. Two finite-element discretizations for gradient elasticity. *Journal of Engineering Mechanics ASCE*, 135(3):203–213, 2009. doi: 10.1061/(ASCE)0733-9399(2009)135:3(203).

[15] J. Petera and J.F.T. Pittman. Isoparametric Hrmite elements . *Inter-*

national *Journal for Numerical Methods in Engineering*, 37:3489–3519, 1994.

[16] A. Zervos, P. Papanastasiou, and I. Vardoulakis. A finite elements displacement formulation for gradient elastoplasticity. *International Journal for Numerical Methods in Engineering*, 50:1369–1388, 2001.

[17] A. Zervos, P. Papanastasiou, and I. Vardoulakis. Modelling of localisation and scale effect in thick-walled cylinders with gradient elastoplasticity. *International Journal of Solids and Structures*, 38:5081–5095, 2001.

[18] S. A. Papanicolopulos, A. Zervos, and I. Vardoulakis. A three-dimensional C^1 finite element for gradient elasticity. *International Journal for Numerical Methods in Engineering*, 77:1396–1415, 2009. doi: 10.1002/nme.2449.

[19] F. Cirak, M. Ortiz, and P. Schröder. Subdivision surface: a new paradigm for thin-shell finite-element analysis. *International Journal for Numerical Methods in Engineering*, 47:2039–2072, 2000.

[20] C. Q. Ru and E. C. Aifantis. A simple approach to solve boundary-value problems in gradient elasticity. *Acta Mechanica*, 101:59–68, 1993. doi: 10.1007/BF01175597.

[21] L. Tenek and E. C. Aifantis. A two-dimensional finite element implementation of a special form of gradient elasticity. *Computer Modeling in Engineering & Sciences*, 3:731–741, 2002.

[22] E. C. Aifantis. On the role of gradients in the localization of deformation and fracture. *International Journal of Engineering Science*, 30(10):1279–1299, 1992. doi: 10.1016/0020-7225(92)90141-3.

[23] S.B. Altan and E. C. Aifantis. On the structure of the mode III crack-tip in gradient elasticity. *Scripta Metallurgica et Materialia*, 26:319–324, 1992.

[24] M. Gutkin and E. C. Aifantis. Edge dislocation in gradient elasticity. *Scripta Materialia*, 36:129–135, 1997.

[25] M. Gutkin and E. C. Aifantis. Dislocations in the theory of gradient elasticity. *Scripta Materialia*, 40:559–566, 1999.

[26] M. Gutkin. Nanoscopics of dislocations and disclinations in gradient elasticity. *Reviews on Advanced Materials Science*, 1:27–60, 2000.

[27] O.C. Zienkiewicz and R.L. Taylor. *The Finite Element Method*, volume 1 – The Basis. Butterworth-Heinemann, 5th edition, 2000. ISBN 0 7506 5049 4.

[28] F. Ihlenburg and I. Babuška. Finite Element Solution of the Helmholtz Equation with High Wave Number Part I: The h-Version of the FEM. *Computers & Mathematics with Applications*, 30(9):9–37, 1995.

[29] L. F. Richardson. The approximate arithmetical solution by finite differences of physical problems involving differential equations, with an application to the stresses in a masonry dam. *Philosophical Transactions of the Royal Society of London A: Mathematical, Physical and En-*

gineering Sciences, 210(459-470):307–357, 1911. ISSN 0264-3952. doi: 10.1098/rsta.1911.0009.